Payri, R.; Gimeno, J.; Marti-Aldaravi, P.; Viera, A. (2021). Measurements of the mass allocation for multiple injection strategies using the rate of injection and momentum flux signals. International Journal of Engine Research. 22(4):1180-1195. https://doi.org/10.1177/1468087419894854

R. Payri et al. "Measurements of the mass allocation for multiple injection strategies using the rate of injection and momentum flux signals", *International Journal of Enigne Research*, First Published On-line, January 6, 2020. DOI: 10.1177/1468087419894854

Measurements of the mass allocation for multiple injection strategies using the rate of injection and momentum flux signals

Raúl Payri, Jaime Gimeno, Pedro Martí-Aldaraví and Alberto Viera

Abstract

As legislations set very stringent environmental and fuel economy standards, researchers have pushed into a continuous development in all areas of the diesel engine. The recent evolution of the injection technologies has permitted to modify the fuel-delivery strategies. From what was a single pulse per injection event, modern systems allow to inject up to 8 different times precisely per combustion cycle. In such sense, experimental results of the rate of injection and momentum flux could be useful for validation and improvement of computational models. Moreover, accurately quantifying the injected mass per pulse in a fuel-gas interface can provide data with more realistic engine-like conditions. To this end, this research presents measurements of the rate of injection and momentum flux for two simple multiple injection strategies: a pilot-main, and a main-post. Boundary conditions included two rail and discharge pressures, two different pilot/post quantities and four dwell times. A new approach was employed to estimate the mass allocation with the momentum flux data, and results were compared to the rate of injection traces to verify the distribution calculated. On the results, signals for each pulse were successfully decoupled using its rising and falling edge. The shot-to-shot variability of the pilot/post injection was highly dependent on its transitory characteristics, and on the dwell time for post injections due to internal pressure waves. The injected mass per pulse was successfully measured as well in the momentum flux test rig, and the energizing time changed slightly to account for the different operation interfaces. Signals from both measurement campaigns showed a remarkable agreement when compared, ascertain the possibility of measuring the injected mass, and its allocation for multiple injection strategies, in the momentum flux test rig.

Keywords

Diesel injection, rate of injection, momentum flux, multiple injection strategies.

Introduction

In recent times, diesel engines are being subject to public scrutiny[1–3]. Legislations have set very stringent environmental and fuel economy standards, that have pushed researchers into a continuous development in all of its areas, and have set the diesel engine as the most efficient alternative[4,5].

One of the main areas is the study of the diesel spray mixing, as it has been recognized as a critical factor in combustion control and the reduction of its related contaminants[6,7]. The characteristics of fuel sprays are conditioned by many parameters, such as the injection pressure, engine load, nozzle geometry[8], and rate of injection, among others. Kim et al.[9] deeply investigated the differences between a direct-acting piezo electric injector and an in-direct one. They found that the faster response and higher fuel injection rates of the direct-acting unit led to a reduction in the combustion heat release and in the in-cylinder pressure, while generating more un-burned emissions. However, when a pilot injection strategy was used, the better control of the direct-acting injector allowed better performance of the engine (faster combustion process). The effect of the injection shape on combustion characteristics and in-cylinder pressure profiles was also investigated by Tay et al.[10], in this case using computational tools. They showed that not only the start of combustion can be controlled just by modifying the injection shape, also the pressure rise and even the liquid impingement on the cylinder head and piston surfaces.

Thus, the spray development is naturally a very complex phenomenon, due to the numerous mechanisms involved and its intrinsically stochastic behavior. Over the years, researchers have studied fuel sprays thoroughly to understand the fundamental processes and establish a reliable experimental set of data that enables the validation of more detailed numerical models[11]. In such sense, computational fluid dynamics (CFD) provide unmatched advantages that coherently complement experimental measurements, as they offer detailed spatial information of complex variables[12] with a high temporal resolution. Moreover, the predictive capabilities of validated CFD models can help to reduce testing times and production costs. However, these are limited to high-fidelity experimental data for validation, and accurate delimitation of the problem.

Recently, the evolution of the injection technologies has permitted not only to improve the spray mixing process, but to control injection parameters accurately, adding flexibility to the systems for new strategies[13,14], and an extra degree of complexity to the researchers. From what previously was a single pulse per combustion cycle, modern systems allow to inject up to 8 different times precisely[13]. To this end, multiple injection strategies have demonstrated to be capable of reducing fuel consumption, particulate matter, carbon oxides, nitrogen oxides, soot, and unburned hydrocarbons[15–23].

CMT - Motores Térmicos, Universitat Politècnica de València, Edificio 6D, 46022, Valencia, Spain.

Corresponding author:
Raúl Payri
Email: rpayri@mot.upv.es

Experimental results could prove useful for validation and improvement of simple spray models[24–26], as well as zero-dimensional models that calculate the rate of injection signals for numerous boundary conditions[27–30]. Furthermore, needle dynamics may differ in the momentum flux test rig because of the changes in the interface from fuel-fuel to fuel-gas[31–33]. Thus, it is essential to quantify the injected mass and its allocation in engine-like conditions, especially in highly transient pulses such as small pilot/post injections. Accordingly, this paper presents measurements of the rate of injection and momentum flux for two simple multiple injection strategies: a pilot-main, and a main-post. Boundary and operating conditions between test cells were kept constant. A two-scale system was used in the rate of injection campaign to verify the values obtained by an upstream scale, that was later implemented to measure the injected mass in the momentum flux facility. A new approach was employed to estimate the mass allocation with the momentum flux data, and results were compared to the rate of injection signals to verify the distribution calculated.

This paper is divided into four sections. Following this introduction, the experimental facilities and measurement methodologies are detailed. Then, results and discussions are presented, organized by the different measurement campaigns that were carried out. In the last section, the main conclusions are drawn.

Materials and Methods

This section presents the test matrix, experimental equipment and data processing methodology for multiple injection strategies, including the approach used to estimate the mass allocation in the momentum flux test rig.

Test matrix

Conditions for the hydraulic characterization were selected to analyze the influence between two injection events: a pilot before the main injection or the main injection on a post. A test group consisted of a single injection event with fixed boundary conditions, and then two different pilot/post quantities and four hydraulic dwell times. Each group was assessed for two rail and discharge pressures, to analyze the influence of boundary conditions on the multiple injection strategies. The test plan is presented in Table 1.

Table 1. Test plan for the hydraulic characterization campaign.

Parameter	Value	Units
Rail pressure (P_r)	100 - 200	MPa
Discharge pressure (P_b)	3 - 6	MPa
Operating temperature	363	K
Pilot/post dwell times	200 - 350 - 500 - 650	µs
Pilot/post inj. quantity	1 - 3	mg
Total mass per inj.	30	mg
Injection frequency	1	Hz
Cycles measured	50	-

The proposed test matrix consists of 40 test points for the hydraulic characterization, with two repetitions per condition. Rail and discharge pressures were selected

considering engine-relevant conditions and Engine Combustion Network (ECN) guidelines[34]. The typical injection frequency for the rate of injection measurements is 10 Hz[35–37], but it was lowered to 1 Hz to use the same value throughout the different test cells, as the heat produced by the piezo stack as well as the operating temperature of the crystal can affect its dynamic response, and thus, modify the injected quantity of the pilot/post pulses[37,38]. The total injected mass was selected accounting for a nozzle with a total nominal flow area of 0.06283 mm^2 installed in 1.6 L engine that injects 50 mg. The pilot/post mass distributions were chosen considering typical engine values of 5 $\%$ and 10 $\%$ of the total injected mass, although in the first case it was reduced to 1 mg to amplify the difference between injected quantities. Dwell times were selected considering a minimum hydraulic separation between injection pulses of 200 µs, increasing it by increments of 150 up to 650 µs.

The injector was driven with a two-stage voltage signal per injection pulse. The signal is comprised of a boost stage to aid needle lift, and then a hold-off stage that controls injection duration. Voltage levels and ramp-off (volts per second) were provided by the original equipment manufacturer (OEM), and they depend on the injection pressure. The signals are depicted in the rate of injection results.

Fuel delivery system

Fuel needs to be delivered to the test chamber at a specific pressure. Additionally, its conditions need to be stable, to some extent, through a wide range of operating points. To this end, the injection system is composed of commercially available components adapted for laboratory use. The main elements are a fuel supply source, a high-pressure unit, a common-rail, and the injector.

Fuel was first purged and filtered, to remove air and particles. Then, it was pressurized by a high-pressure (HP) pump powered by an electric motor. A common-rail fitted with a pressure regulator was connected to the high-pressure outlet of the pump, used as a control unit. The regulator was driven with a closed-loop proportional-integral-derivative (PID) commercial controller. Low-pressure fuel returning from the common-rail and the pump was cooled down with a heat exchanger, and sent to the air purger along with the fuel back-flow from the injector. A flexible line transported the pressurized fuel from the control common-rail to the corresponding test rig. Figure 1 presents a schematic diagram of the high-pressure unit.

The injector used is the latest iteration of a commercially available piezo common-rail (PCR) type 5 from Continental[13]. It has a micro piezo stack actuator, which compared to the conventional ones, maximizes the internal high-pressure volume, improving its efficiency in multiple injection strategies. Besides, the piezo stack is powerful enough to handle operating injection pressures up to 250 MPa. The injector was fitted with a six hole nozzle, with its main characteristics summarized in Table 2.

Rate of injection configuration

Mass flow rate measurements were carried out with an Injection Rate Discharge Curve Indicator (IRDCI) from IAV. It measures the rate of injection (ROI) with the long-tube method, whose working principle is based on the theory of pressure wave propagation in a liquid column. The setup used is presented as a schematic diagram in Figure 2. Fuel

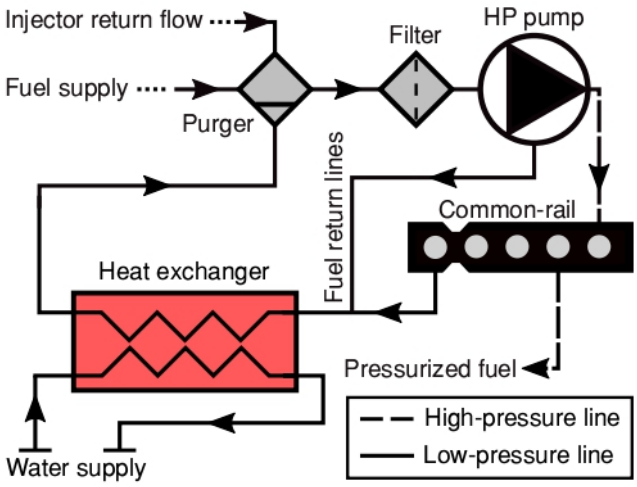

Figure 1. High-pressure unit schematic diagram.

Table 2. Real nozzle geometry.

Parameter	Value	Units
Number of orifices	6	-
Avg. outlet diameter ($\overline{D}_o$)	90.1*	μm
Outlet diameter (D_o)	91.7**	μm
Avg. *k-factor*	5.3	-
Nominal flow rate	313***	$\mathrm{mL\,min^{-1}}$
Avg. height angle	74.8	
Degree of hydro-erosion	7.7	%

* Considering all orifices.
** Of the orifice measured in the momentum flux test rig.
*** At 10 MPa of injection pressure.

was supplied to the high-pressure unit (sketched in Figure 1) by a vase mounted on an upstream scale. Then, the pressurized fuel was delivered from this high-pressure unit to a second common-rail (volume = 22 $\mathrm{cm^3}$, length = 28 cm), and fed to the injector through a high-pressure rigid line (inside/outside diameter = 2.4/6 mm, length 24 cm). The rail and line configurations were selected to comply with ECN standards[34]. Fuel exited the IRDCI, and it was deposited into a downstream scale. The quantity injected was measured by both scales, accounting for the number of injections in a period of 120 seconds. The injector was commanded by a manual piezo pulse signal generator, which replaces the engine control unit (ECU).

The dynamic response of the piezo stacks is very dependent on its working temperature[38,39], and therefore it could affect the hydraulic performance of the injector[37]. Accordingly, the injector was mounted to the IRDCI with a special holder that allows controlling its operating temperature. The holder had a cooling sleeve that extended along the body of the injector, with a thermocouple inserted in the middle to

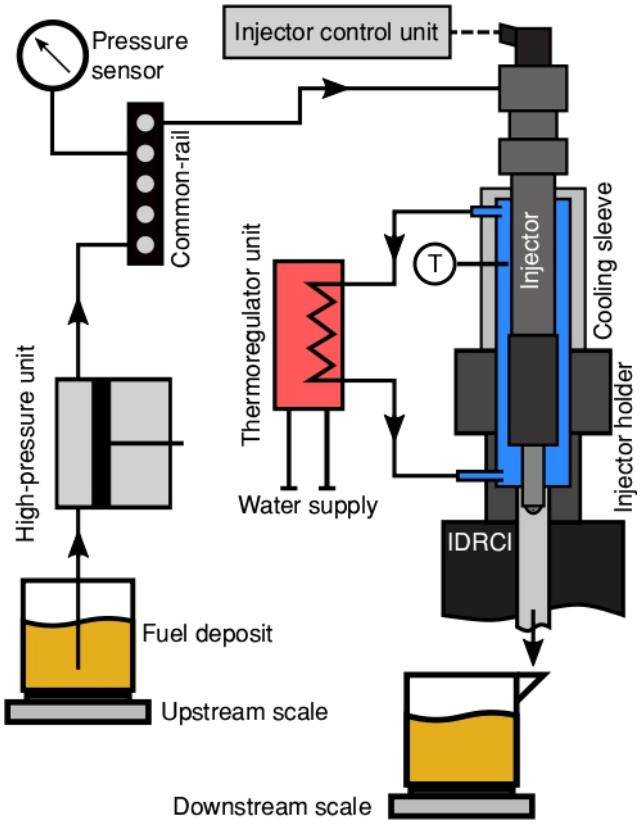

Figure 2. Schematic diagram of the setup used for the rate of injection measurements.

monitor the temperature. This system was driven by a thermoregulator unit that used ethylene glycol at 30 %, pumped at a rate of up to 60 $\mathrm{L/\,min}$, heated by a 6 kW unit, and cooled down by a separate water supply system.

A digital oscilloscope records the rate of injection, rail pressure, and driving voltage signals, for a total of 50 injections per test point at a rate of 1 injection event per second. The time reference of the measurement, that is $t = 0$, is the start of energizing (SOE) of the injector. All the data is directly averaged, and then the ROI is corrected for the signal accumulation phenomenon, with a methodology thoroughly described by Payri *et al*[35]. The shot to shot dispersion is measured through the standard deviation of all the data[36], and it is below 1% in all cases during the whole injection duration.

The final signal is then integrated to obtain the injected mass. Due to the uncertainties in the calculation of the speed of sound, cycle-to-cycle and temperature variations, among others, the integral of the rate of injection signal can differ from the mass measured by the scale. Thus, a standard methodology was developed in the laboratory and used in many previous publications[35–37,40,41]. A scaling factor is calculated with

the ratio of the mass measured by the downstream unit divided by the integrated mass, and is multiplied with the averaged signal.

Momentum flux configuration

Part of the setup used to measure momentum flux is presented in Figure 3. The same fuel supply scheme as previously shown was used to provide the fuel to the injector, so the injected mass can be measured with the upstream scale. The injector was mounted in the test rig with the same cooling sleeve unit, to keep the temperature of operation constant throughout measurements and experimental facilities. The pressure transducer, which captures the impact force, was installed into a specific holder that positions the sensor perpendicularly to the spray axis. A spacer was used to control its distance to the outlet of the nozzle. Additionally, a set of shims that act as spacers between the injector holder and the test rig can be used to control the vertical position of the injector referenced to the sensor (with the same orientation as in the figure), but it was not necessary for this configuration. Chamber pressure is controlled by a set of valves that regulate the inlet and outlet flow of nitrogen.

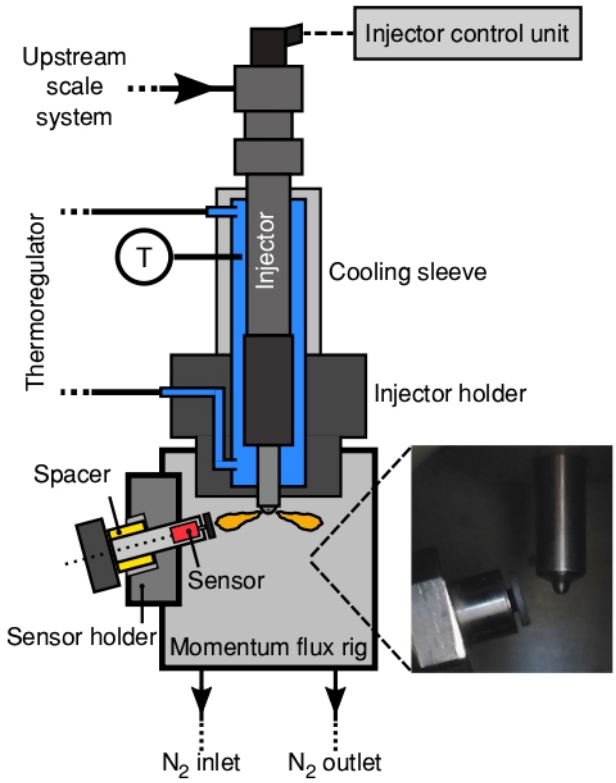

Figure 3. Schematic diagram of the setup used for the momentum flux measurements.

As in the rate of injection measurements, a digital oscilloscope records the momentum flux, rail pressure, and driving voltage signals, for a total of 50 injections per test point at a rate of 1 injection event per second. The average signal, is corrected for the accumulation phenomenon[35], and the injected mass is verified with the upstream scale.

Data processing

As the number of pulses increases in an injection event, it is necessary to decouple each process to quantify their respective injected mass. Accordingly, for rate of injection results, the start and end of injection for each pulse were calculated with the rising and falling edge of each curve following the procedure of Salvador et al.[40]. Then the injected mass was estimated by integrating each of the pulses within these limits, and the total mass adding these values. An example of the result obtained is depicted in Figure 4. Note that the dwell time was measured from the end of injection of the first pulse to the start of injection of the second pulse.

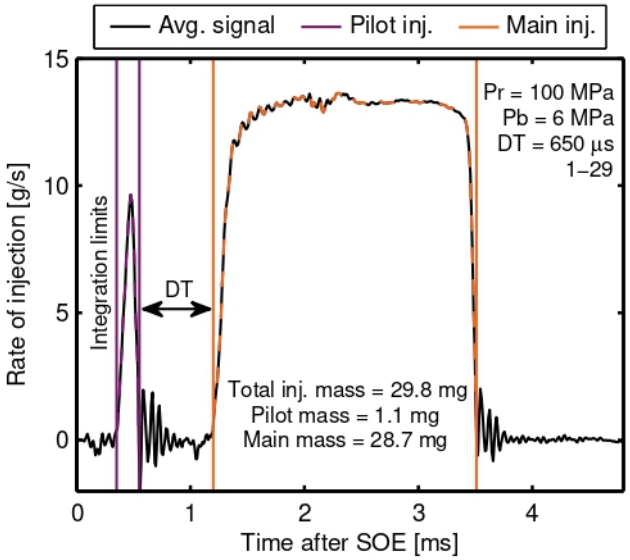

Figure 4. Example of the decoupling of two injection pulses and their respective injected quantities. The labeling 1-29 refers to the nominal strategy of 1 mg and 29 mg for the injected mass of pilot and main pulses respectively.

The nominal strategy is presented with a label (for example, $1-29$ in the figure) that refers to the target mass of the pilot and main injection, while the order of these numbers refers to either a pilot-main or a main-post case. This labeling structure is maintained throughout the document. For multiple injections, the energizing time of the first pulse was kept for fixed conditions of injected mass and different dwell times. However, because of the rail pressure drop induced by the first injection pulse, and the pressure waves that appear within the injector, the energizing time of the second pulse

had to be slightly modified when the dwell time was changed, to maintain the target of a total injected mass of 30 mg per injection event.

For momentum flux, the total injected mass is measured by the upstream scale. However, to estimate its allocation for multiple injection pulses, a link to the rate of injection is found in the basic definition of both variables, extracted from the work by Payri *et al*[42]:

$$\dot{m} = A \cdot \rho_f \cdot u \tag{1}$$

$$\dot{M} = A \cdot \rho_f \cdot u^2 \tag{2}$$

Where $\dot{m}$ is the rate of injection, A is the area, ρ_f is the density of the fuel, u is the velocity, and $\dot{M}$ is the momentum flux. In the presence of cavitation, the area and velocity terms can be changed to a simplified flow model with an effective area and velocity[42]. Solving the velocity, the rate of injection and momentum flux can be related with the following expression:

$$\sqrt{\dot{M}} \approx \frac{\dot{m}}{\sqrt{A \cdot \rho_f}} \tag{3}$$

Considering that boundary conditions were kept equal along experimental vessels, Equation 3 provides a direct link between the ROI and momentum flux ($\sqrt{\dot{M}} \propto \dot{m}$). Therefore, the mass injected by each pulse was calculated as the area allocation, after integrating the square root of the momentum signal. An example is shown in Figure 5, where for a strategy of 1-29 mg, that represents a nominal area distribution of 3.3 $\%$ - 96.7 $\%$ for a target mass of 30 mg, the area integrated from the square root of the momentum signal has to match that ratio.

Needle dynamics can change in momentum flux test rig because the interface varies from fuel-fuel to fuel-gas[31–33], and the injection quantity and its distribution might differ slightly. Each injection pulse was decoupled with the same procedure as in the rate of injection, with the rising and falling edge of each signal. Then, with the total injected mass per cycle, the quantity by each pulse can be estimated (and multiplied by the number of holes as previously discussed), and the energizing times slightly corrected to achieve the target mass. Note that the SOI and EOI are not the same as in the injection rate measurements, due to the time it takes for the spray to impact the sensor.

Results and discussion

This section presents the results of the complete hydraulic characterization for multiple injection strategies.

Rate of injection for multiple injection strategies

Rate of injection results are presented in a set of three vertical subplots that consist of the driving signal (top), rail pressure measurement (middle), and rate of injection (bottom). All results are always compared with their baseline point, which is at the

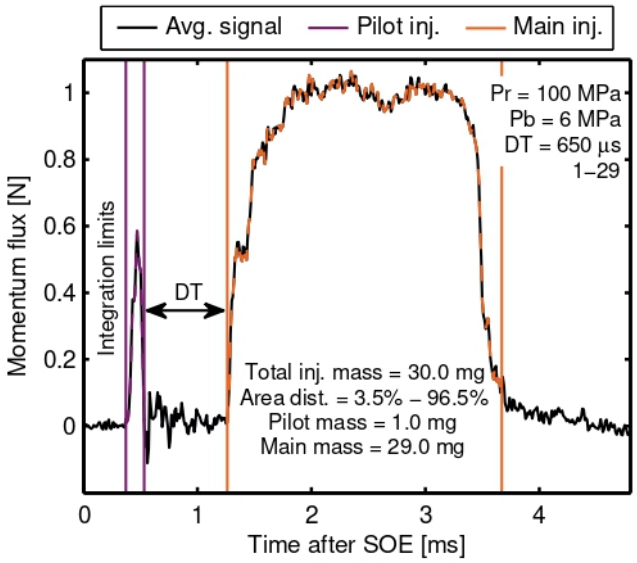

Figure 5. Example of the allocation of the injected mass in the momentum flux test rig. The area was calculated as the integral of the square root of the momentum flux signal for each injection pulse.

same conditions of rail and discharge pressure, and named "Single" (or with zero dwell time) as it has no multiple injections. Rail pressure signals were phased to their nominal level for comparison purposes. Nevertheless, the differences in rail pressure levels before injection between test points were less than 1%, thanks to a robust pressure control system.

In Figures 6, 7, 8 and 9 results of the rate of injection for the different pilot injection masses and rail pressures are depicted. Each color represents a hydraulic dwell time. Due to the high number of test points carried out, only one discharge pressure is presented for each rail pressure, as it is well-known that it has little influence in the hydraulic performance of the injector[35,36,40,42].

For both rail pressures and the smallest pilot quantities, the injector did not achieve a stabilized operation and ran entirely in a transitory state through this first injection event. When the pilot quantity increased to 3 mg, stable conditions were reached but not with a fully developed flow, probably due to the sac pressure loss during the start of the injection process[33,40,43–45]. Sac pressure decreases mainly for two reasons: the volume of the displaced needle that is filled with fuel from its surroundings, plus the fuel that is injected into the chamber. Thus, even though the needle reached lift levels where it does not have any influence on the internal flow development, fully developed flow conditions are not reached until sac pressure recovers[45].

Additionally, at lower rail pressures, closed-couple pilots produced a faster rate of the start of injection for the main event, probably due to the effect of pressure waves within the injector sac and control volume[33,46–48]. This was quantified by calculating the average start of injection speed as the maximum opening slope of the curve for

the conditions presented in the previous plot, and results are shown in Figure 10. The impact of the pressure waves can be somewhat visualized in the ROI signal, as local oscillations are observed at the beginning of the main injection signal for the shorter dwell cases, and they get smoother when increasing the dwell time. Thus, as a general consequence, the main injection needed a shorter driving signal to achieve the same mass quantity with decreasing dwell time. However, the total energizing time, compared to the single injection case, needed to be longer in order to reach the target injected mass of 30 mg due to the added hydraulic delay of each new injection pulse.

Examples of the results regarding post injections are depicted in Figures 11, 12, 13 and 14. As with the pilot injections, a similar behavior was observed. For the smallest post quantities, the injector did not achieve a stabilized operation and ran entirely in a transitory state through this second injection event. Consequently, the control of the mass quantity of the smaller post injection was rather difficult, because the performance of the injector is affected by the impact of the pressure waves in the transient of the needle, that depends on the rail pressure. This explain as well the different trends of the post injected quantity with decreasing dwell time observed in Figure 11 and

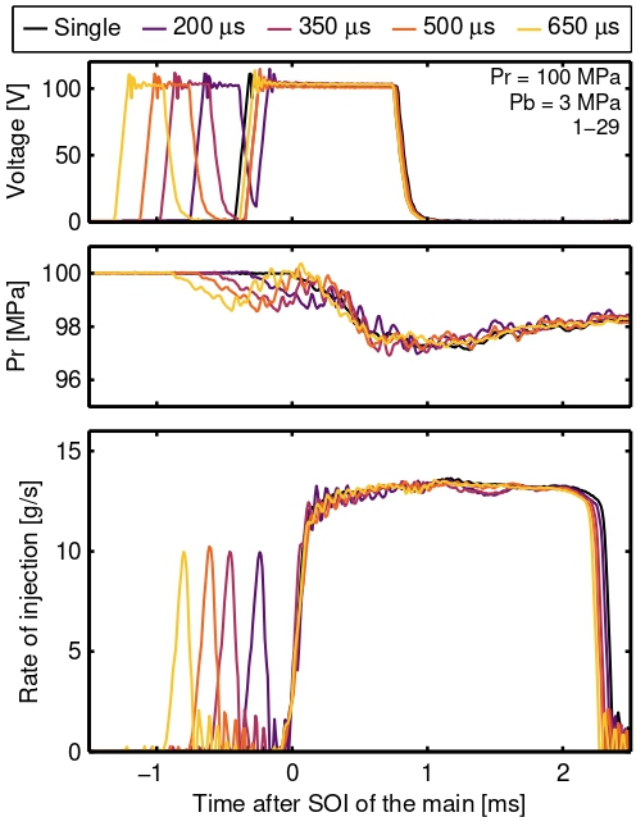

Figure 6. Driving signal (top), rail pressure (middle) and rate of injection (bottom) measured for a pilot injection quantity of 1 mg, and a rail pressure of 100 MPa.

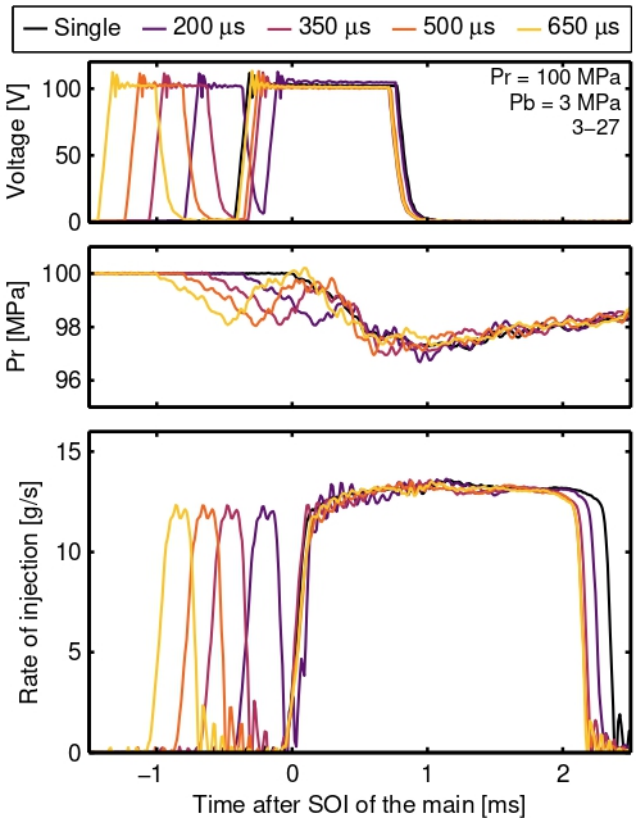

Figure 7. Driving signal (top), rail pressure (middle) and rate of injection (bottom) measured for a pilot injection quantity of 3 mg, and a rail pressure of 100 MPa.

Figure 13. Moreover, in pilot-main strategies, the SOI velocity of the second pulse was affected by the pilot injection, as the first pulse had no prior event altering its hydraulic performance. Thus, the same effect is observed on main-post strategies, but much amplified as this second pulse is entirely transitory. A similar conclusion was reached in the work of Carreres[43], where the pressure within the control volume was calculated through 1-D modeling, and the effect of pressure waves in the performance of post injections was quantified.

Altogether, the pilot/post target mass of 1 mg were managed with a 10 $\%$ deviation, with some specific conditions measuring overshoots of up to 20 $\%$. However, this is a combination of the precision of both the injector and the measurement system. For the target mass of 3 mg, pilot/post injection quantities were attained within a reasonable deviation of under 5 $\%$, with some outliers above this value. The total target mass of 30 mg was achieved in general with deviations below 2 $\%$.

Nevertheless, one of the main challenges of multiple injection strategies is the control of the pilot/post pulses, especially when quantities are small, because the injector operates only in a transitory state, as seen in the previous results. To this end,

a shot-to-shot dispersion analysis was carried out to observe in which conditions the injector operates with a considerate variability. The relative standard deviation (RSD) was calculated as the standard deviation of the integrated mass (m_{int}) for each pulse of the 50 cycles, divided by the value for the integrated mass of the averaged signal, that is:

$$RSD = 100\ \frac{std([m1_{int}\ m2_{int}\ m3_{int}\ ...\ m50_{int}])}{m_{int}} \qquad [\%] \tag{4}$$

Therefore, Equation 4 represents the ratio of the standard deviation to the mean value in a percentual scale. Results regarding the dispersion of the pilot-main strategies are presented in Figure 15. Single injection cases, depicted as the data with zero dwell time, show the lowest RSD of all. The highest deviation was observed for the pilot masses of 1 mg, as expected due to its transient behavior. For such cases, the determinant factor is probably the needle closing time, which can slightly differ if the closing phase starts during the transitory start of injection. Moreover, the dispersion, being close to the accuracy of the measurement, is higher with 200 MPa than 100 MPa. It means that

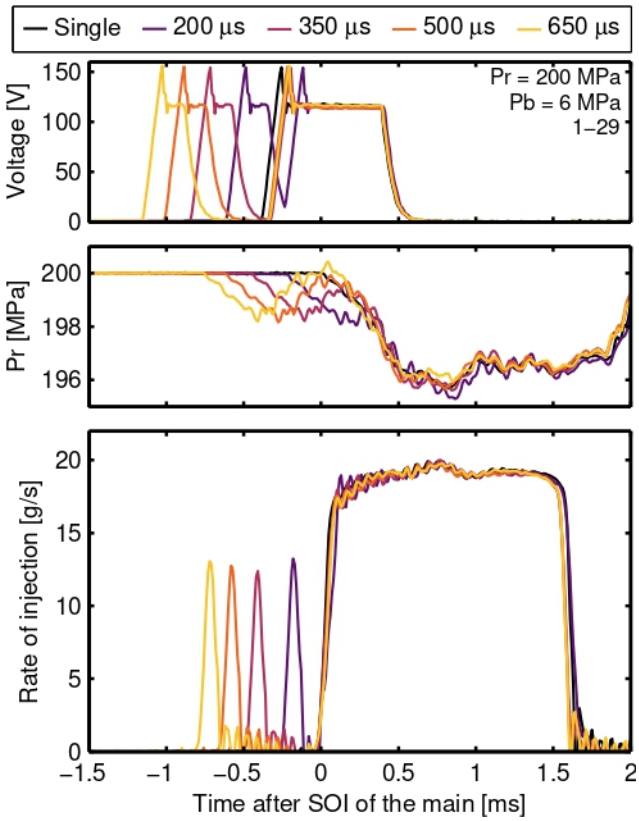

Figure 8. Driving signal (top), rail pressure (middle) and rate of injection (bottom) measured for a pilot injection quantity of 1 mg, and a rail pressure of 200 MPa.

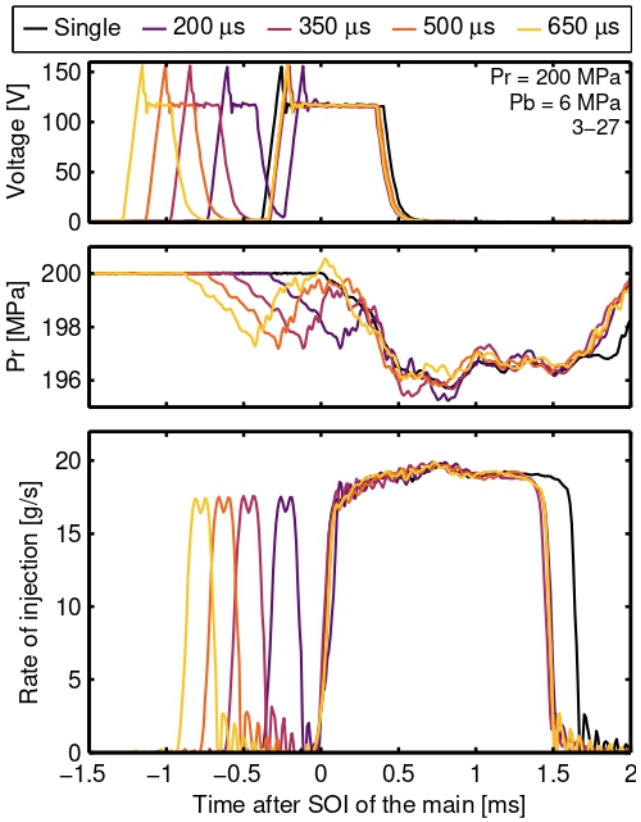

Figure 9. Driving signal (top), rail pressure (middle) and rate of injection (bottom) measured for a pilot injection quantity of 3 mg, and a rail pressure of 200 MPa.

injection control difficulty increases as well. Note that the deviations observed for these cases are within the reported dispersion for the measured pilot mass in the previous section. When the pilot mass is increased to 3 mg, RSD decreases significantly, but still, values calculated are higher than their respective reference case of a single injection. The trend regarding the rail pressure is reversed, probably because at 200 MPa stationary conditions are reached faster as the SOI velocity is higher (Figure 10). For each pilot-main case, their corresponding main injection is depicted with filled symbols. When including a pilot mass, the variability of the main injection marginally increases compared to the reference case, probably due to pressure waves within the sac of the nozzle affecting the dynamic of the needle for the second pulse [15,33,43,48].

Results regarding the dispersion of the main-post strategies are presented in Figure 16. Once again, the lowest RSD values were obtained for the reference single injection cases, and the main pulses (filled symbols) that correspond to the main event of a post injection at a specific value of rail pressure and dwell time. These injections are non perturbed by any prior event and have the same behavior as the reference case. Overall, deviations values for the post mass were higher than those

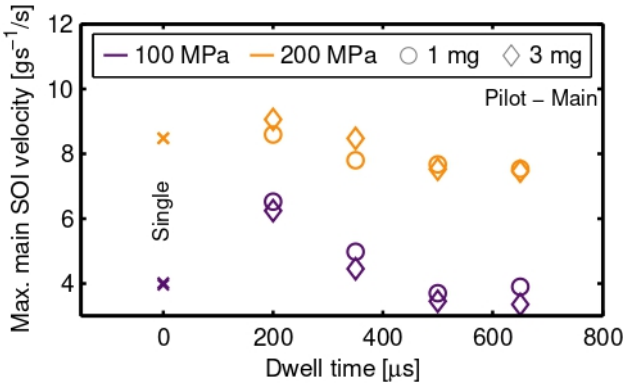

Figure 10. Start of injection speed of the main pulse event, calculated as its maximum opening slope, for different pilot quantities and dwell times. Data is compared to a single injection event, represented with a null dwell time.

obtained for pilot-main strategies, as the pressure drop and waves generated by the main pulse have a substantial impact in the transients of the post injections. In addition, as observed in the previous figure, increasing the post quantity also decreases the shot-to-shot dispersion at fixed conditions of rail pressure and dwell time, probably because partially stable operations are reached. Interestingly, for a fixed dwell time, if less shot-to-shot dispersion was achieved at lower rail pressure for a 1 mg post injected mass, the same trend is observed for the 3 mg quantity, highlighting the influence of pressure waves in the injection control for post-pulses[15,43]. The highest RSD was attained for 1 mg and 200 µs of dwell time. At these conditions, the short dwell between pulses probably does not provide enough time for the pressure within the nozzle to partially stabilize, and thus, as the injector is operating in a fully transitory state, pressure waves or transients, that might vary for each cycle, have a more significant impact on the cycle-to-cycle dispersion of the post injection.

Validation of the upstream scale

A two-scale configuration was used to also monitor the injected mass in the momentum flux test rig. The standard procedure in the laboratory for ROI measurements is to use the downstream scale to verify and correct the injected quantity of the integrated signal obtained from the IRDCI[35,37]. A device located upstream is prone to depend on changes in fuel properties. For example, it was observed that when the fuel in the purger heats up and expands slowly, the scale can measure smaller values compared to the downstream device, in where fuel properties remain constant to some extent. Thus enough time was given for the upstream fuel to reach somewhat stable conditions. Differences between scales are depicted in Figure 17.

In general, the percentual error between scales was less than 5 %, with some outlying values of up to 10 %. Differences between scales are probably related to the variations induced by the different number of elements, mass flow and fuel lines from the upstream unit to the injector, and from the injector to the downstream unit.

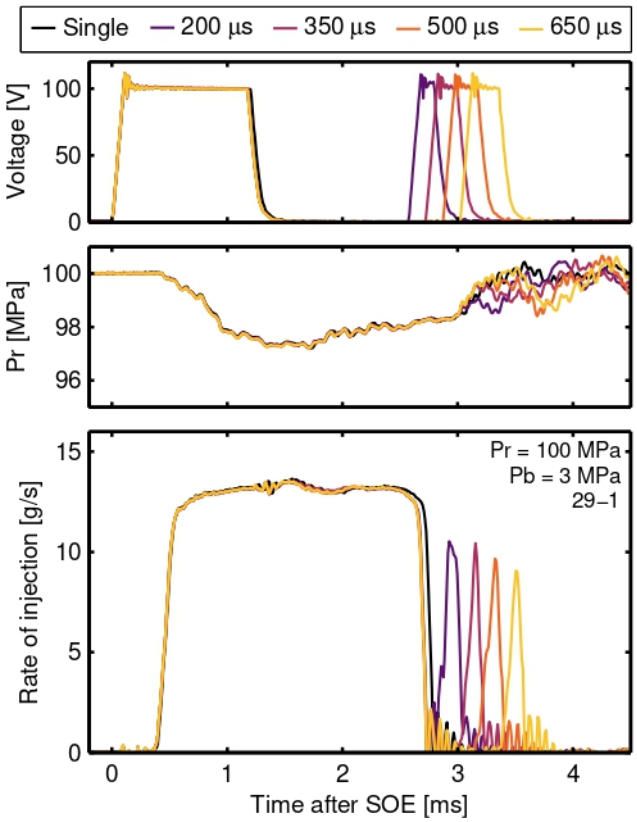

Figure 11. Driving signal (top), rail pressure (middle) and rate of injection (bottom) measured for a post injection quantity of 1 mg, and a rail pressure of 100 MPa.

Hole-to-hole performance for single injections

The mass allocation presented in the rate of injection results considers that all the holes of the nozzle perform equally. In the momentum flux campaign, the upstream scale quantified the total injected mass per cycle, but only one spray was measured in multiple injection conditions (labeled spray of interest). Thus, a hole-to-hole comparison was carried out to verify the mass distribution. The spray studied was compared along with two of other five sprays of the nozzle (labeled number 3 and 5), by rotating the injector holder and aligning each with the pressure sensor. Only single injection conditions were measured, for the same rail and discharge pressures as in the previous cases. Results are summarized in Figure 18.

From the figure, the spray of interest performs at par with the other two plumes, both in the transitory and stabilized regions. Therefore, the real injected mass per hole can be approximated to the measured quantity by the upstream scale divided by the total number of holes. Nevertheless, even though only the spray of interest was measured in the momentum flux rig with multiple injection strategies, the injected quantities

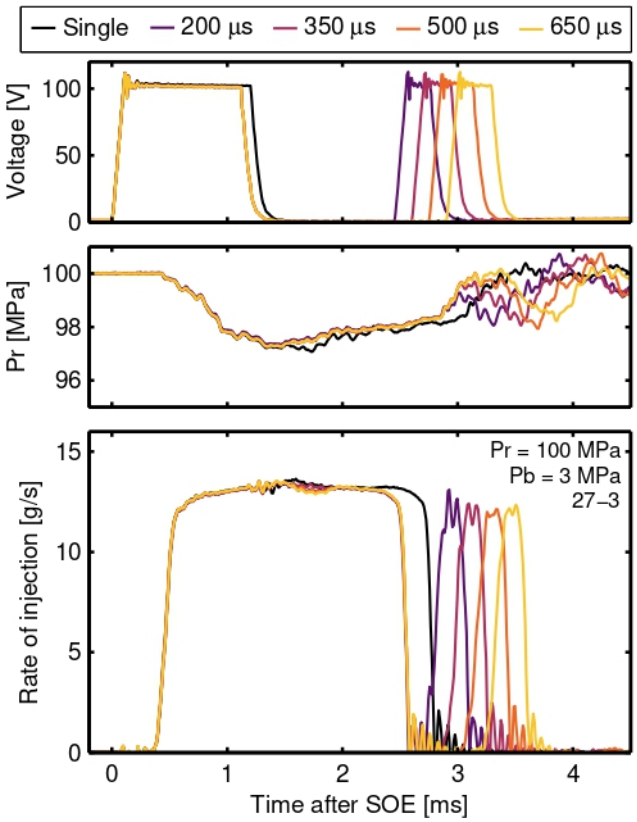

Figure 12. Driving signal (top), rail pressure (middle) and rate of injection (bottom) measured for a post injection quantity of 3 mg, and a rail pressure of 100 MPa.

calculated in this section were scaled to maintain the same labeling structure throughout the document.

Momentum flux for multiple injection strategies

Momentum flux results are presented, along with the rail pressure, in the same plotting structure as in the previous section. All results are always compared with their baseline point, which is at the same conditions of rail and discharge pressure, named “Single” (or with zero dwell time) as it has no pilot/post injections. Rail pressure signals were phased to their nominal level for comparison purposes.

In Figures 19, 20, 21 and 22 results of the momentum flux for the different pilot injection masses and rail pressures are depicted. Each color represents a hydraulic dwell time.

In general, the results resemble trends observed in the rate of injection measurements, and total momentum is now distributed throughout the multiple pulses. The signal shows a localized step in the rising edge, characteristic of the momentum

lost by the head of the spray while accelerating the stationary gas in the initial phase of mixing[42,49,50]. Therefore the interpretation of the results has to consider that the distance from the nozzle tip to the sensor modifies the signal in such way, that it does not precisely represent the momentum flux at the outlet of the nozzle. For a rail pressure of 100 MPa, the corresponding start of injection of the main pulse correlates well to the measured dwell times and pilot quantities. Stabilized conditions are also reached for the 3 mg pilot, but for a shorter period due to the initial momentum loss, as the duration of this main injection is shorter. Increasing the rail pressure induced more noise in the transient of the main signal, and the start and end of injection curves are not as smooth as in the previous case. With increasing injection pressure, both flow velocity and rate of air entrainment are higher[51]. Therefore the first injection pulse induces turbulence in the control volume that might slightly affect the signal of the main pulse.

Example of the results regarding post injections are depicted in Figures 23, 24, 25 and 26. As before, similar trends to ROI results were observed. For the smallest post quantities, the injector does not achieve a stabilized operation and runs entirely in a transitory state. Therefore, once again, controlling the injected mass was difficult

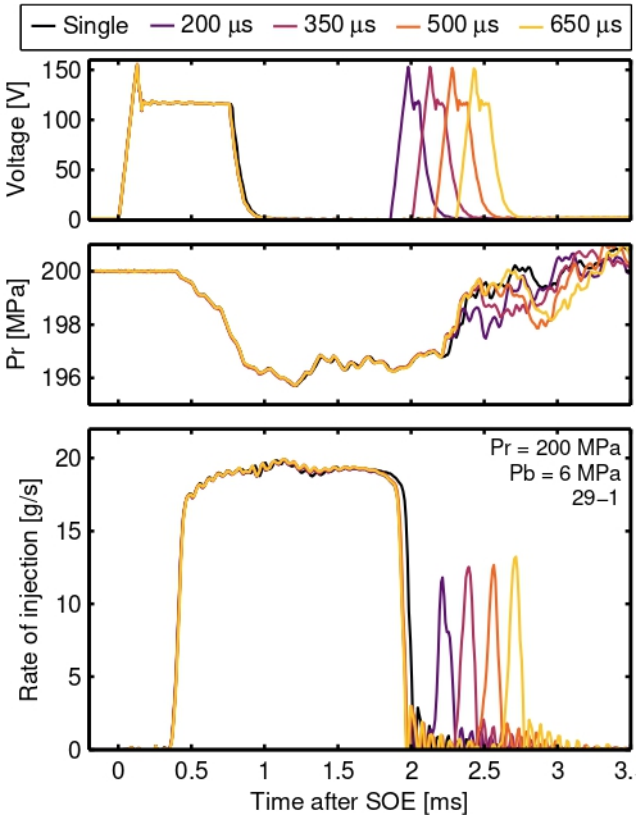

Figure 13. Driving signal (top), rail pressure (middle) and rate of injection (bottom) measured for a post injection quantity of 1 mg, and a rail pressure of 200 MPa.

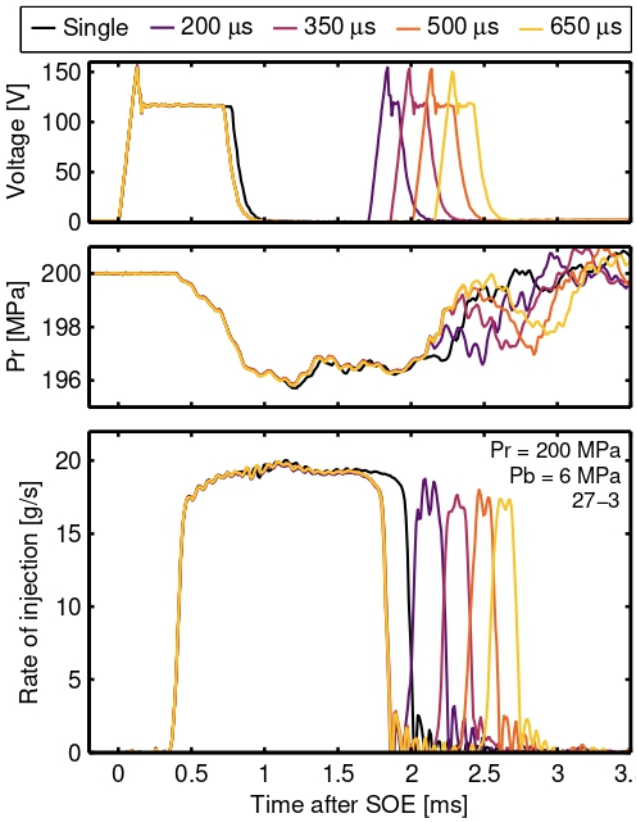

Figure 14. Driving signal (top), rail pressure (middle) and rate of injection (bottom) measured for a post injection quantity of 3 mg, and a rail pressure of 200 MPa.

compared to post injection with a target mass of 3 mg, where a stable operation regime was reached. As a consequence, post injection quantities of 1 mg presented the highest deviation from the target value.

Altogether, the pilot and post target mass of 1 mg were managed with a deviation between 10 $\%$ and 20 $\%$, an acceptable tolerance considering that momentum flux is not measured directly at the orifice outlet. For the target mass of 3 mg, pilot and post injection quantities were attained with deviations of around 5 $\%$ to 10 $\%$. The total mass of 30 mg was achieved overall with values within 2 $\%$ of the target. Note that these results consider the mass measured by the upstream scale, that is the injected quantity through all the holes of the nozzle.

Verifying the mass distribution with both signals

Quantifying the mass in the momentum flux test rig presented challenges, because the spray impacts the pressure sensor downstream from the outlet of the nozzle, producing the initial momentum loss mentioned in the previous section. This is somewhat

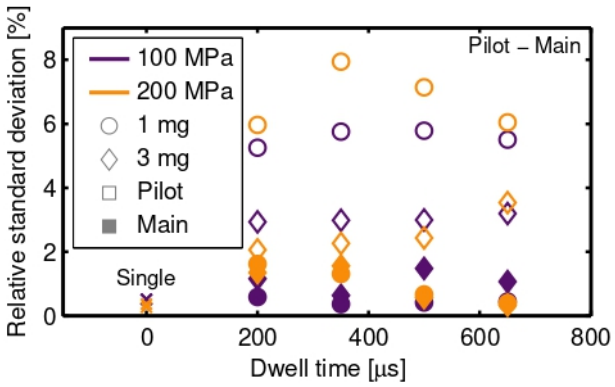

Figure 15. Relative standard deviation of the rate of injection results presented in the previous section for pilot-main strategies. Different symbols represent either the single injection or each of the injected quantities of the pilot pulse. Filled symbols depict the main injection associated with a pilot mass at a specific rail pressure and dwell time.

.

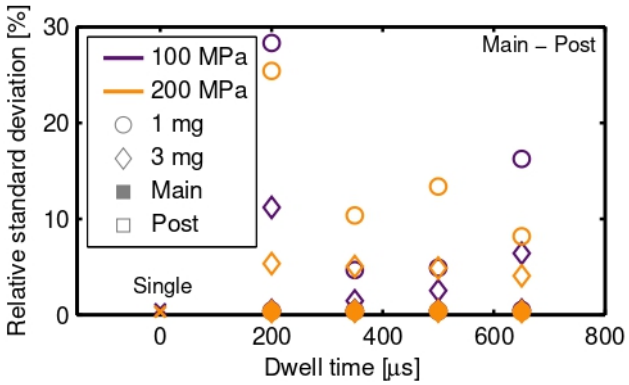

Figure 16. Relative standard deviation of the rate of injection results presented in the previous section for main-post strategies. Different symbols represent either the single injection or each of the injected quantities of the post pulse. Filled symbols depict the main injection associated with a post mass at a specific rail pressure and dwell time.

.

recovered when the inertia of the liquid fuel and the gas entrained, still in the control volume, impacts the sensor after the end of injection[42]. Therefore, the location of the end of the injection in the momentum flux signal is difficult to estimate.

Thus, to verify the quantified injected mass and its allocation obtained in the momentum flux test rig, results were compared to the rate of injection curves previously depicted. A momentum flux signal was estimated from the ROI data using the simplification of Equation 3, considering the the value of the signal measured in the momentum flux test cell, and the density of the fuel calculated using the correlation presented by Payri *et al*[52] for commercial diesel fuel, with the temperature measured by

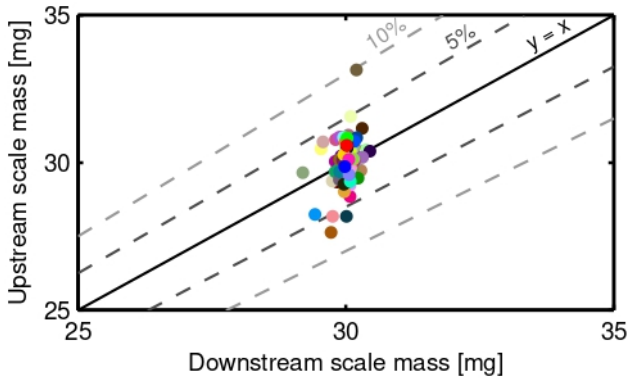

Figure 17. Masses measured with the downstream scale (x-axis) and the upstream scale (y-axis). The dashed lines define a 5 % and 10 % deviation.

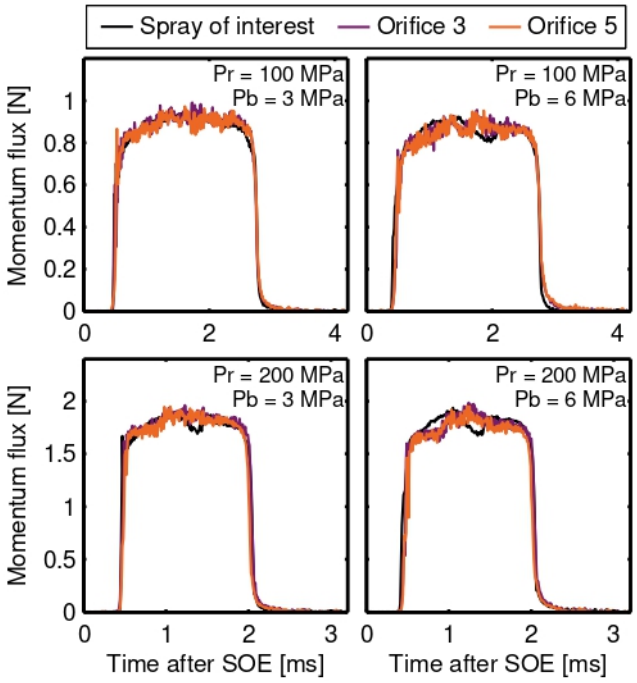

Figure 18. Hole-to-hole comparison for different rail and discharge pressure with a single injection.

a thermocouple located in the discharge section. Additionally, for each test condition, the momentum flux was phased with the rate of injection data, to counteract the delay of the spray going through the control volume and impacting the sensor. Examples for the same pilot injections at two different rail pressures are presented in Figures 27 and

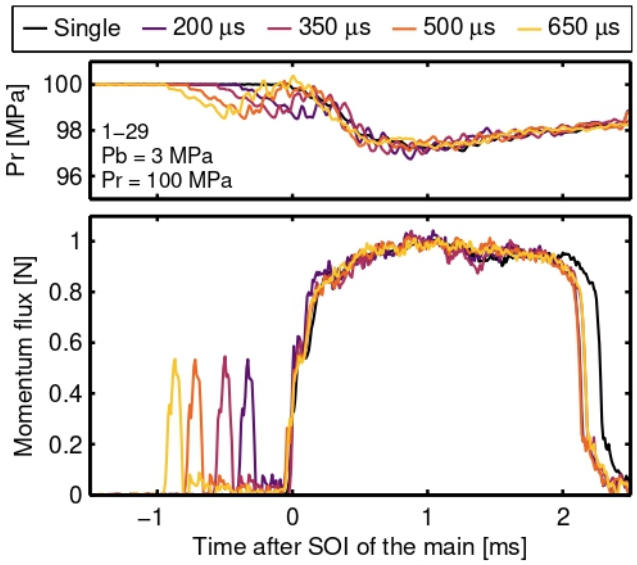

Figure 19. Rail pressure (top) and momentum flux (bottom) measured for a pilot injection quantity of 1 mg, and a rail pressure of 100 MPa.

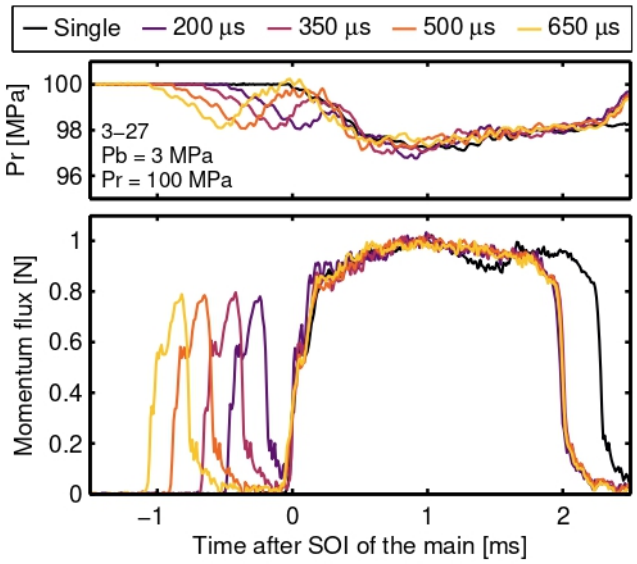

Figure 20. Rail pressure (top) and momentum flux (bottom) measured for a pilot injection quantity of 3 mg, and a rail pressure of 100 MPa.

28, whereas examples of both post quantities at two different rail pressures are depicted in Figures 29 and 30.

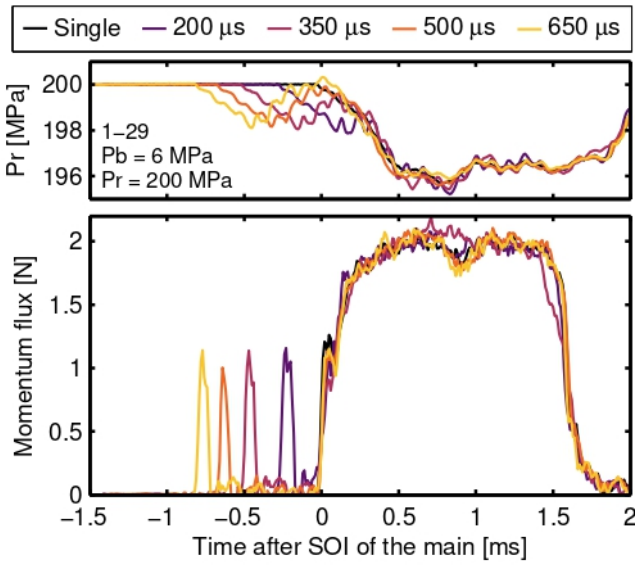

Figure 21. Rail pressure (top) and momentum flux (bottom) measured for a pilot injection quantity of 1 mg, and a rail pressure of 200 MPa.

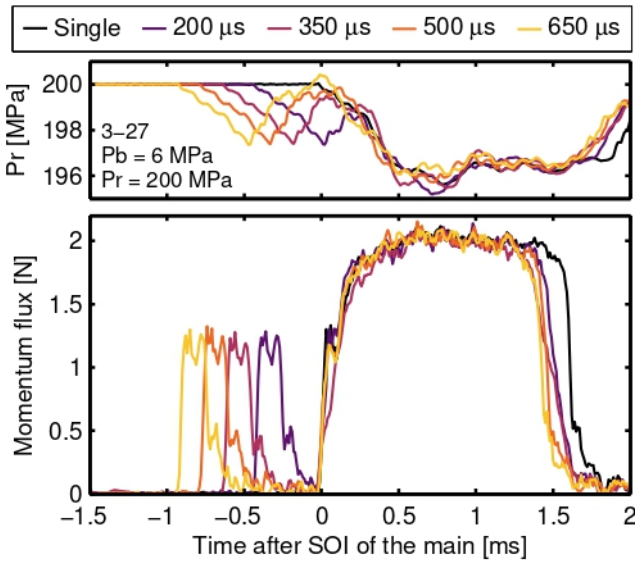

Figure 22. Rail pressure (top) and momentum flux (bottom) measured for a pilot injection quantity of 3 mg, and a rail pressure of 200 MPa.

In general, results from both experimental data sets showed remarkable agreement with the approximation proposed. Pilot/post injections of 1 mg that are all performed

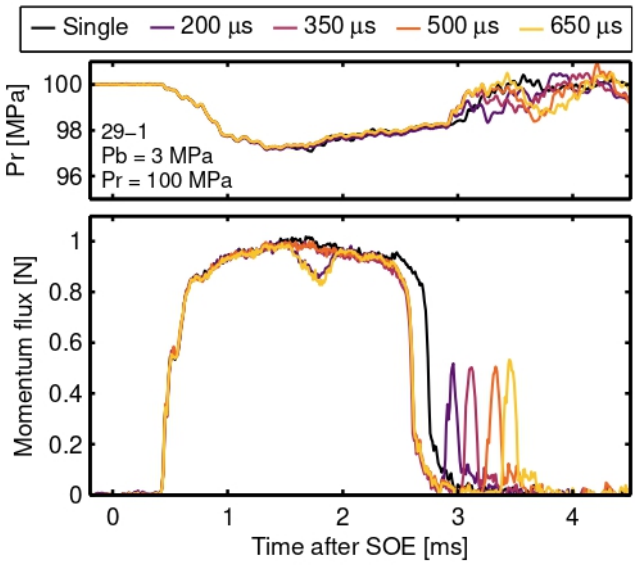

Figure 23. Rail pressure (top) and momentum flux (bottom) measured for a post injection quantity of 1 mg, and a rail pressure of 100 MPa.

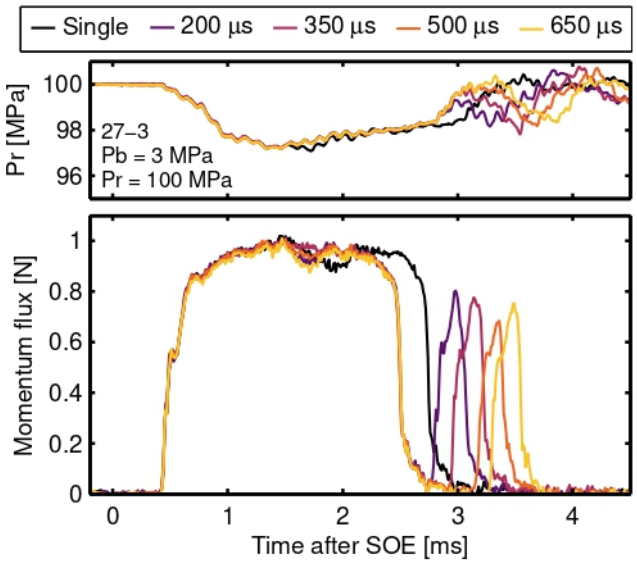

Figure 24. Rail pressure (top) and momentum flux (bottom) measured for a post injection quantity of 3 mg, and a rail pressure of 100 MPa.

in a transitory stage resemble quite notably in shape and phasing. However, for the main-post strategy, the transition between injections was affected by the momentum

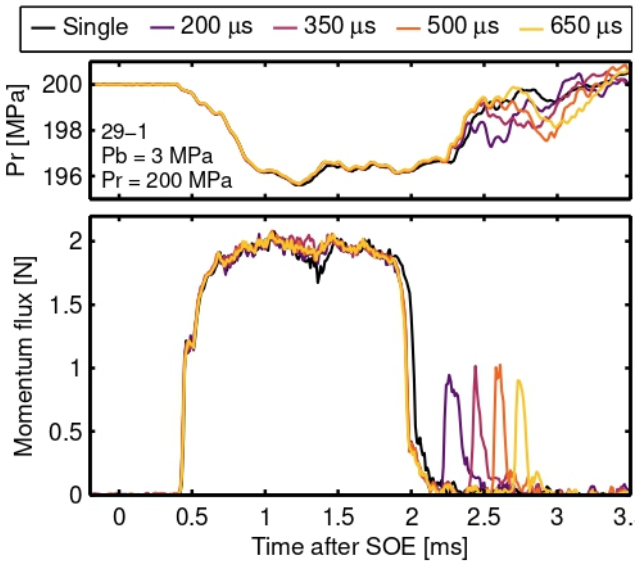

Figure 25. Rail pressure (top) and momentum flux (bottom) measured for a post injection quantity of 1 mg, and a rail pressure of 200 MPa.

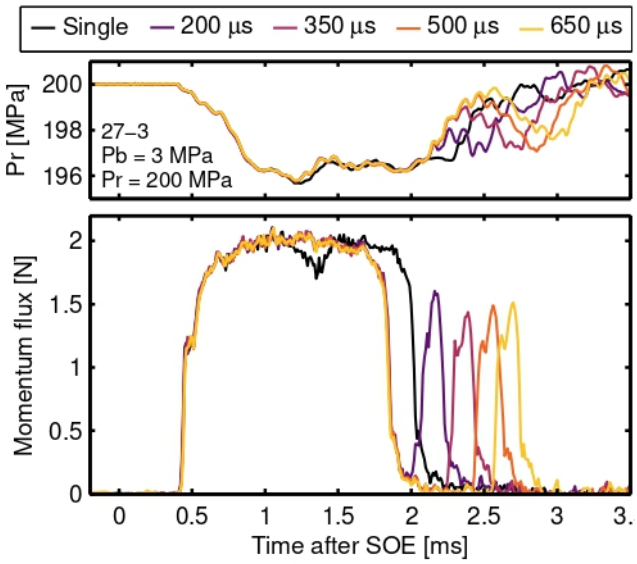

Figure 26. Rail pressure (top) and momentum flux (bottom) measured for a post injection quantity of 3 mg, and a rail pressure of 200 MPa.

recovery at the end of injection of the main pulse. But the resemblance with the rate of injection results confirms that the hydraulic dwell times were estimated correctly.

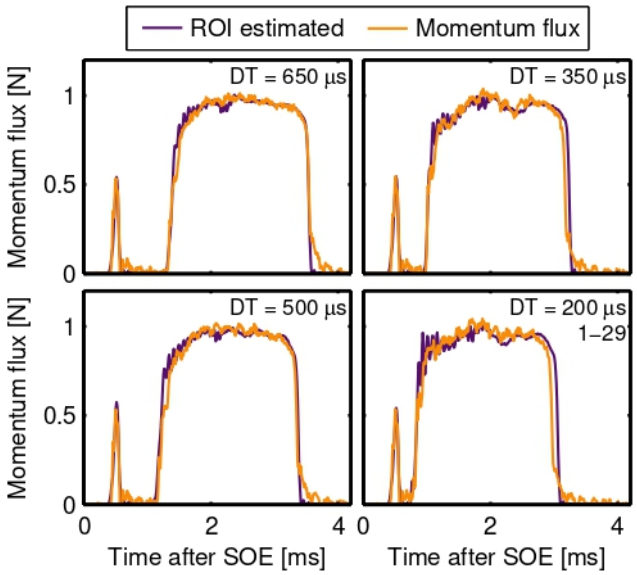

Figure 27. Scaled rate of injection and momentum flux signals for a pilot quantity of 1 mg, a rail pressure of 100 MPa, and a discharge pressure of 3 MPa.

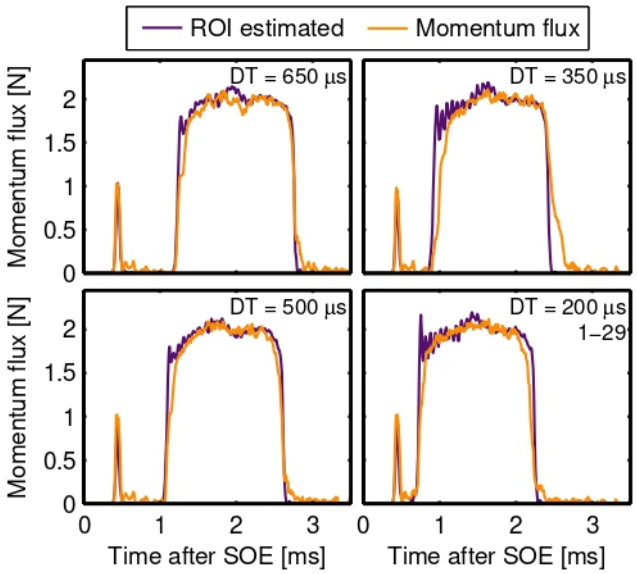

Figure 28. Scaled rate of injection and momentum flux signals for a pilot quantity of 1 mg, a rail pressure of 200 MPa, and a discharge pressure of 3 MPa.

For a post injected quantity of 3 mg, signals are still phased correctly in time, but the

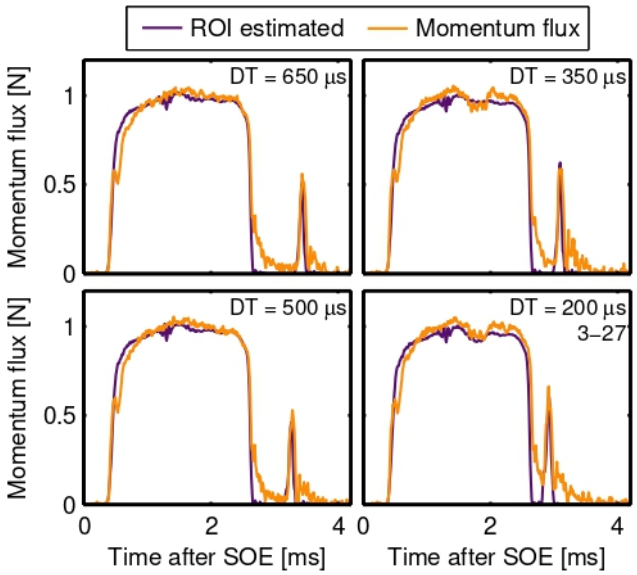

Figure 29. Scaled rate of injection and momentum flux signals for a post quantity of 1 mg, a rail pressure of 100 MPa, and a discharge pressure of 6 MPa.

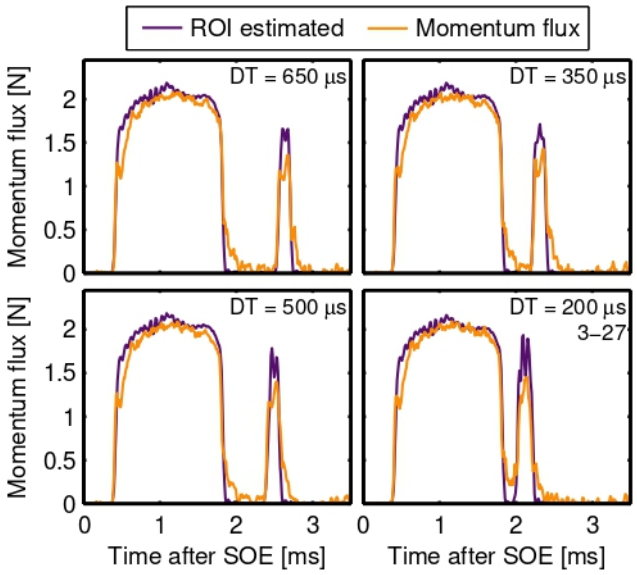

Figure 30. Scaled rate of injection and momentum flux signals for a post quantity of 3 mg, a rail pressure of 200 MPa, and a discharge pressure of 6 MPa.

momentum curve falls short of the local maximum. This trend was observed for most of the 3 mg pilot/post injections, and is probably due to the initial momentum loss.

The excellent coherence between the data depicted in the figures proves the robustness of the methodology employed. Also, it ascertains the possibility of measuring the injected mass and its allocation (for multiple injection strategies) in the momentum flux rig, and remarks that operating conditions of the injector were correctly controlled and maintained throughout experimental vessels.

Summary and conclusions

In this paper, measurements of the rate of injection and momentum flux were carried out for a 6-hole nozzle using two simple multiple injection strategies: a pilot-main and a main-post. The rate of injection campaign included a two-scale system to quantify the injected mass and its allocation between the pilot/post and main pulse, and also the differences between both scales. Additionally, a novel methodology was developed with an upstream scale to estimate the injected mass and its allocation in the momentum flux test rig for multiple injection strategies.

From the rate of injection results:

- Signals from multiple pulses were properly decoupled using the rising and falling of each injection pulse. Mass distribution was calculated as the integral of each injection.
- For an injected mass of $1\ \mathrm{mg}$ for both pilot-main or main-post strategies, the injector did not achieve a stabilized operation and ran entirely in a transitory state. When the pilot/post quantity was increased to $3\ \mathrm{mg}$, a stable operation was achieved.
- For the lower rail pressure, decreasing the dwell time between the first and second pulses produced a faster start of injection of the second event, with a maximum value observed for 200 µs. Increasing the rail pressure reduced the dynamic influence between injections, though no significant effect was observed.
- Injection control for the pulse of $1\ \mathrm{mg}$ and 200 µs of dwell time in main-post strategies showed high cycle variability, because of the impact of the pressure waves produced by the first injection, especially since the second event is all transient. Increasing the injected quantity improved shot-to-shot dispersion.
- In general, both pilot and post target mass of $1\ \mathrm{mg}$ and $3\ \mathrm{mg}$ were attained with deviations between 10% and 5% respectively, with some specific points as outliers. The total mass was achieved with values within 2% of the target.
- The values measured by the scale located upstream of the test rig were affected by changes in the temperature of the fuel. However, after enough time was provided for the fuel to reach steady conditions, the scale quantified the injected mass with deviations of generally less than 5% compared to the downstream unit.

From the momentum flux results:

- Signals were properly decoupled using the rising and falling of each injection pulse. Mass allocation was calculated with the area distribution by integrating the square root of the momentum flux signal, matching the ratio of each area with the injected mass.

- Overall, results resembled the trends observed in the rate of injection measurements. The signal showed a step in the rising edge, characteristic of the momentum lost by the head of the spray while accelerating the stationary gas in the control volume. Also, it depicted a rebound on the falling edge due to the inertia of the liquid fuel and gas entrained in the control volume impacting the sensor after the end of injection.
- Pilot/post injections of $1\ \mathrm{mg}$ were performed fully in a transitory state for both strategies. As a consequence, injection control for the second pulse in the main-post sequence turned difficult as in ROI. Contrarily, the signal reached the stabilized region when increasing the injected mass to $3\ \mathrm{mg}$.
- In general, pilot/post injections with a target mass of $1\ \mathrm{mg}$ were managed with variations between 10% and 20%, respectively. For $3\ \mathrm{mg}$, deviation lowered to the range of $5\ \%$ to $10\ \%$, respectively. The total mass was achieved with values within 2% of the target.

Both series of results were compared to verify the quantification of the allocation of the mass in the momentum flux measurements. An estimated momentum flux was obtained from the rate of injection data and compared to the real momentum flux signal, which was phased to counteract the delay of the spray traveling through the control volume before impacting the sensor.

Overall, the results showed remarkable agreement. For the main-post strategy, the transition between pulses was slightly affected by the momentum recovery at the end of the injection of the main pulse. But the resemblance with the rate of injection results confirms that the hydraulic dwell times were estimated correctly. For most of the $3\ \%$ pilot/post injections, signals are phased, but the momentum curve falls short of the local maximum, probably due to the initial momentum loss.

The excellent coherence between the data proves the robustness of the methodology employed. Also, it ascertains the possibility of measuring the injected mass and its allocation, especially for multiple injection strategies, in the momentum flux rig.

Acknowledgements

This research has been partially funded by the Spanish Ministerio de Ciencias, Investigación y Universidades through project RTI2018-099706-B-I00. Part of the experimental hardware was purchased through funds obtained from Generalitat Valenciana and FEDER through project IDIFEDER/2018/037. Additionally, Alberto Viera is supported through the FPI contract 2016-S2-1361 of “Programa de Apoyo para la Investigación y Desarrollo (PAID)” of Universitat Poltècnica de València.

References

1. Steinparzer F, Stütz W and Brüne Hj. Reliable, efficient and environmentally friendly: The new BMW Diesel engines with RDE technology. In Eichlseder H and Wimmer A (eds.) *16th Conference The Working Process of the Internal Combustion Engine*. Graz: Verlag der Technischen Universität Graz, pp. 15–22.

2. Reitz RD, Ogawa H, Payri R et al. IJER editorial: The future of the internal combustion engine. *International Journal of Engine Research* 2019; Editorial: 1–8. DOI:10.1177/1468087419877990.
3. Payri R, Serrano JR, Tormos B et al. An objective reflection about the potential future of diesel vehicles against arguments based on energy populism. *DYNA* 2019; 94(5): 480–482. DOI:10.6036/9245.
4. Johnson TV. Diesel engine emissions and their control. *Platinum Metals Review* 2008; 52(1): 23–37. DOI:10.1595/147106708X248750.
5. Johnson TV. Diesel Emission in Review. *SAE Technical Paper 2011-01-0304* 2011; DOI: 10.4271/2011-01-0304.
6. Musculus MPB, Miles PC and Pickett LM. Conceptual models for partially premixed low-temperature diesel combustion. *Progress in Energy and Combustion Science* 2013; 39(2-3): 246–283. DOI:10.1016/j.pecs.2012.09.001.
7. Han S, Kim J and Bae C. Effect of air-fuel mixing quality on characteristics of conventional and low temperature diesel combustion. *Applied Energy* 2014; 119: 454–466. DOI: 10.1016/j.apenergy.2013.12.045.
8. Payri R, De La Morena J, Monsalve-Serrano J et al. Impact of counter-bore nozzle on the combustion process and exhaust emissions for light-duty diesel engine application. *International Journal of Engine Research* 2019; 20(1): 46–57. DOI:10.1177/1468087418819250.
9. Kim J, Kim J, Jeong S et al. Effects of different piezo-acting mechanism on two-stage fuel injection and CI combustion in a CRDi engine. *Journal of Mechanical Science and Technology* 2016; 30(12): 5727–5737. DOI:10.1007/s12206-016-1143-0.
10. Tay KL, Yang W, Zhao F et al. Effects of triangular and ramp injection rate-shapes on the performance and emissions of a kerosene-diesel fueled direct injection compression ignition engine: A numerical study. *Applied Thermal Engineering* 2017; 110: 1401–1410. DOI: 10.1016/j.applthermaleng.2016.09.072.
11. Fansler TD and Parrish SE. Spray measurement technology: a review. *Measurement Science and Technology* 2015; 26(1): 012002. DOI:10.1088/0957-0233/26/1/012002.
12. Payri R, Gimeno J, Martí-Aldaraví P et al. A new approach to compute temperature in a liquid-gas mixture. Application to study the effect of wall nozzle temperature on a Diesel injector. *International Journal of Heat and Fluid Flow* 2017; 68: 79–86. DOI: 10.1016/j.ijheatfluidflow.2016.12.008.
13. Schöppe D, Stahl C, Krüger G et al. Servo-Driven Piezo Common Rail Diesel Injection System. *ATZ Autotechnology* 2012; 12(2): 42–47. DOI:10.1365/s35595-012-0107-y.
14. Yazdani K, Amani E and Naderan H. Multi-objective optimizations of the boot injection strategy for reactivity controlled compression ignition engines. *International Journal of Engine Research* 2019; 20(8-9): 889–910. DOI:10.1177/1468087418795599.
15. Badami M, Mallamo F, Millo F et al. Influence of Multiple Injection Strategies on Emissions, Combustion Noise and BSFC of a DI Common Rail Diesel Engine. *SAE Technical Paper 2002-01-0503* 2002; DOI:10.4271/2002-01-0503.
16. Beatrice C, Belardini P, Bertoli C et al. Diesel Combustion control in common rail engines by new injection strategies. *International Journal of Engine Research* 2002; 3(1): 23–36. DOI:10.1243/1468087021545513.
17. Carlucci P, Ficarella A and Laforgia D. Effects on combustion and emissions of early and pilot fuel injections in diesel engines. *International Journal of Engine Research* 2005; 6(1):

43–60. DOI:10.1243/146808705X7301.

18. Mingfa Y, Hu W, Zunqing Z et al. Experimental Study of Multiple Injections and Coupling Effects of Multi-Injection and EGR in a HD Diesel Engine. *SAE Technical Paper 2009-01-2807* 2009; DOI:10.4271/2009-01-2807.
19. Lee J, Jeon J, Park J et al. Effect of Multiple Injection Strategies on Emission and Combustion Characteristics in a Single Cylinder Direct-Injection Optical Engine. *SAE Technical Paper 2009-01-1354* 2010; DOI:10.4271/2009-01-1354.
20. O'Connor J and Musculus MPB. Effects of exhaust gas recirculation and load on soot in a heavy-duty optical diesel engine with close-coupled post injections for high-efficiency combustion phasing. *International Journal of Engine Research* 2014; 15(4): 421–443. DOI: 10.1177/1468087413488767.
21. O'Connor J, Musculus MPB and Pickett LM. Effect of post injections on mixture preparation and unburned hydrocarbon emissions in a heavy-duty diesel engine. *Combustion and Flame* 2016; 170: 111–123. DOI:10.1016/j.combustflame.2016.03.031.
22. Park C and Busch S. The influence of pilot injection on high-temperature ignition processes and early flame structure in a high-speed direct injection diesel engine. *International Journal of Engine Research* 2018; 19(6): 668–681. DOI:10.1177/1468087417728630.
23. Beatrice C, Di Blasio G, Pesce FC et al. Key fuel injection system features for efficiency improvement in future diesel passenger cars. *SAE Technical Paper 2019-01-0547* 2019; DOI:10.4271/2019-01-0547.
24. Pastor JV, López JJ, García-Oliver JM et al. A 1D model for the description of mixing-controlled inert diesel sprays. *Fuel* 2008; 87(13-14): 2871–2885. DOI:10.1016/j.fuel.2008.04.017.
25. Desantes JM, Pastor JV, García-Oliver JM et al. A 1D model for the description of mixing-controlled reacting diesel sprays. *Combustion and Flame* 2009; 156(1): 234–249. DOI: 10.1016/j.combustflame.2008.10.008.
26. Yamasaki Y, Ikemura R, Takahashi M et al. Simple combustion model for a diesel engine with multiple fuel injections. *International Journal of Engine Research* 2019; 20(2): 167–180. DOI:10.1177/1468087417742764.
27. Payri R, Gimeno J, Novella R et al. On the rate of injection modeling applied to direct injection compression ignition engines. *International Journal of Engine Research* 2016; 17(10): 1015–1030. DOI:10.1177/1468087416636281.
28. Piano A, Millo F, Postrioti L et al. Numerical and Experimental Assessment of a Solenoid Common-Rail Injector Operation with Advanced Injection Strategies. *SAE International Journal of Engines* 2016; 9(1). DOI:10.4271/2016-01-0563.
29. Piano A, Boccardo G, Millo F et al. Experimental and Numerical Assessment of Multi-Event Injection Strategies in a Solenoid Common-Rail Injector. *SAE International Journal of Engines* 2017; 10(4). DOI:10.4271/2017-24-0012.
30. Soriano JA, Mata C, Armas O et al. A zero-dimensional model to simulate injection rate from first generation common rail diesel injectors under thermodynamic diagnosis. *Energy* 2018; 158: 845–858. DOI:10.1016/j.energy.2018.06.054.
31. Manin J, Kastengren AL and Payri R. Understanding the Acoustic Oscillations Observed in the Injection Rate of a Common-Rail Direct Injection Diesel Injector. *Journal of Engineering for Gas Turbines and Power* 2012; 134(12). DOI:10.1115/1.4007276.
32. Pickett LM, Manin J, Payri R et al. Transient Rate of Injection Effects on Spray Development. *SAE Technical Paper 2013-24-0001* 2013; DOI:10.4271/2013-24-0001.

33. Manin J, Pickett LM and Yasutomi K. Transient cavitation in transparent diesel injectors. In *ICLASS 14th Triennial International Conference on Liquid Atomization and Spray Systems*. Chicago, pp. 1–9.
34. Engine Combustion Network. https://ecn.sandia.gov/diesel-spray-combustion/. Online, 2010.
35. Payri R, Salvador FJ, Gimeno J et al. A new methodology for correcting the signal cumulative phenomenon on injection rate measurements. *Experimental Techniques* 2008; 32(1): 46–49. DOI:10.1111/j.1747-1567.2007.00188.x.
36. Payri R, Gimeno J, Cuisano J et al. Hydraulic characterization of diesel engine single-hole injectors. *Fuel* 2016; 180: 357–366. DOI:10.1016/j.fuel.2016.03.083.
37. Payri R, Gimeno J, Mata C et al. Rate of injection measurements of a direct-acting piezoelectric injector for different operating temperatures. *Energy Conversion and Management* 2017; 154: 387–393. DOI:10.1016/j.enconman.2017.11.029.
38. Altieri L and Tonoli A. Piezoelectric Injectors for Automotive Applications: Modeling and Experimental Validation of Hysteretic Behavior and Temperature Effects. *Journal of Dynamic Systems, Measurement, and Control* 2012; 135(1): 011005. DOI:10.1115/1.4006627.
39. Le D, Shen J, Ruikar N et al. Dynamic modeling of a piezoelectric fuel injector during rate shaping operation. *International Journal of Engine Research* 2013; 15(4): 471–487. DOI:10.1177/1468087413492737.
40. Salvador FJ, Gimeno J, Carreres M et al. Fuel temperature influence on the performance of a last generation common-rail diesel ballistic injector. Part I: Experimental mass flow rate measurements and discussion. *Energy Conversion and Management* 2016; 114: 364–375. DOI:10.1016/j.enconman.2016.02.042.
41. Viera JP, Payri R, Swantek AB et al. Linking instantaneous rate of injection to X-ray needle lift measurements for a direct-acting piezoelectric injector. *Energy Conversion and Management* 2016; 112: 350–358. DOI:10.1016/j.enconman.2016.01.038.
42. Payri R, García-Oliver JM, Salvador FJ et al. Using spray momentum flux measurements to understand the influence of diesel nozzle geometry on spray characteristics. *Fuel* 2005; 84(5): 551–561. DOI:10.1016/j.fuel.2004.10.009.
43. Carreres M. *Thermal effects influence on the Diesel injector performance through a combined 1D modelling and experimental approach*. PhD Thesis, Universitat Politècnica de València, 2016. DOI:10.4995/Thesis/10251/73066.
44. Payri R, Salvador FJ, Carreres M et al. Thermal effects on the diesel injector performance through adiabatic 1D modelling. Part II: Model validation, results of the simulations and discussion. *Fuel* 2020; 260. DOI:10.1016/j.fuel.2019.115663.
45. Payri R, Salvador FJ, Carreres M et al. Fuel temperature influence on the performance of a last generation common-rail diesel ballistic injector. Part II: 1D model development, validation and analysis. *Energy Conversion and Management* 2016; 114: 376–391. DOI: 10.1016/j.enconman.2016.02.043.
46. Han JS, Wang TC, Xie XB et al. Dynamics of Multiple-Injection Fuel Sprays in a Small-bore HSDI Diesel Engine. *SAE Technical Paper 2000-01-1256* 2000; DOI:10.4271/2000-01-1256.
47. Baratta M, Catania AE and Ferrari A. Hydraulic Circuit Design Rules to Remove the Dependence of the Injected Fuel Amount on Dwell Time in Multijet CR Systems. *Journal of Fluids Engineering* 2008; 130(12). DOI:10.1115/1.2969443.

48. Payri R, De la Morena J, Pagano V et al. One-dimensional modeling of the interaction between close-coupled injection events for a ballistic solenoid injector. *International Journal of Engine Research* 2019; 20(4): 452–469. DOI:10.1177/1468087418760973.
49. Desantes JM, Payri R, Salvador FJ et al. Measurements of spray momentum for the study of cavitation in diesel injection nozzles. *SAE Technical Paper 2003-01-0703* 2003; DOI: 10.4271/2003-01-0703.
50. Postrioti L, Mariani F, Battistoni M et al. Experimental and Numerical Evaluation of Diesel Spray Momentum Flux. *SAE International Journal of Engines* 2009; 4970(2). DOI: doi.org/10.4271/2009-01-2772.
51. Siebers DL. Liquid-Phase Fuel Penetration in Diesel Sprays. *SAE Technical Paper 980809* 1998; DOI:10.4271/980809.
52. Payri R, Salvador FJ, Gimeno J et al. The effect of temperature and pressure on thermodynamic properties of diesel and biodiesel fuels. *Fuel* 2011; 90(3): 1172–1180. DOI: 10.1016/j.fuel.2010.11.015.